Journal of Materials Chemistry A

ROYAL SOCIETY OF CHEMISTRY

PAPER

View Article Online
View Journal | View Issue

Cite this: J. Mater. Chem. A, 2025, 13, 42281

Unveiling the complexity of co-evaporation of perovskite: Why co-evaporation might not be the optimal choice

Mohamed A. A. Mahmoud, *[abc] Yashika Gupta,[ab] Oliver Fischer, [ab] Jann B. Landgraf,[abd] Martin Bivour[b] and Juliane Borchert [abcd]

Co-evaporation has emerged as a promising deposition method for perovskite solar cells, offering several advantages such as solvent-free processing and scalability. However, in this work, we systematically report the challenges we faced during the thermal co-evaporation of organic–inorganic perovskite precursors to form a double-cation, double-halide wide bandgap perovskite with the composition ($FA_xCs_{1-x}Pb(I_yBr_{1-y})_3$), which may hinder the deposition methods's transfer to industry. We demonstrate that the substrate material plays a crucial role in perovskite formation, where even minor surface treatments, such as annealing or washing (in the case of self-assembled molecules), can substantially influence film properties. More critically, we describe the difficulty in controlling the deposition rates of inorganic precursors in the co-evaporation method due to the non-linear evaporation of the organic component leading to inconsistencies in stoichiometry and irreproducible device performance. These inherent challenges limit the suitability of co-evaporation for systematic studies. Moreover, we show a direct relation between the amount of FAI incorporated in the perovskite film and the formation of a pure alpha phase.

Received 12th October 2025
Accepted 30th October 2025

DOI: 10.1039/d5ta08316h

rsc.li/materials-a

1 Introduction

The full evaporation route for perovskite deposition has been identified as a highly promising approach for the scalable fabrication of perovskite solar cells, owing to its numerous advantages. These advantages include the elimination of hazardous solvents, compatibility with various substrate architectures and the potential for large-scale production.[1–5]

However, a critical examination of the existing literature on the thermal co-evaporation of organic–inorganic perovskite precursors reveals several challenges. Notably, the number of studies on this deposition method remains limited, and reports on device efficiency often exhibit high standard deviations or lack of statistics, with little to no discussion on reproducibility.[6–8] Only a few studies have explored this deposition method in tandem with a silicon bottom solar cell.[6,7,9]

A notable exception is a study by Škorjanc *et al.* that reported a very high standard deviation in its results while proposing a new approach to mitigate these variations.[10] The researchers tested different seed layers prior to the co-evaporation process and demonstrated that by using a few nm of CsCl as a seed layer, the standard deviation of the solar cell efficiencies decreased significantly. Another similar study was reported earlier by Yan *et al.*[4] where they fabricated solar cells incorporating templated $FA_{0.9}Cs_{0.1}PbI_{3-x}Cl_x$ reporting a power conversion efficiency (PCE) over 19.8%.

However, the proposed method introduces another deposition technique known as sequential evaporation. Furthermore, it remains difficult to control the evaporation rates of the other inorganic materials during the FAI deposition process, particularly in regard to potential cross-talk between the different precursors.

Therefore, in this study, we present a detailed investigation of the challenges we encountered in the co-evaporation of organic–inorganic precursors to form a wide bandgap double-cation, double-halide perovskite with the composition ($FA_xCs_{1-x}Pb(I_yBr_{1-y})_3$). These challenges are inherent and a limitation to the co-evaporation deposition method of organic–inorganic precursors.

Building upon previous reports,[6,11–13] we provide an in-depth analysis of the significant influence of different substrate materials on the formation of co-evaporated perovskite films. Additionally, we demonstrate that even minor modifications to the substrate, such as annealing or surface treatment (*e.g.*, washing in the case of self-assembled molecules (SAMs)), substantially impact the perovskite formation. This hinders

[a]Chair for Photovoltaic Energy Conversion, Department of Sustainable Systems Engineering INATECH, University of Freiburg, 79110 Freiburg, Germany
[b]Fraunhofer Institute of Solar Energy Systems, Freiburg, 79110, Germany. E-mail: mohamed.mahmoud@ise.fraunhofer.de
[c]Freiburg Center for Interactive Materials and Bioinspired Technologies, University of Freiburg (FIT), 79110 Freiburg, Germany
[d]Cluster of Excellence livMatS @ FIT – Freiburg Center for Interactive Materials and Bioinspired Technologies, University of Freiburg, 79110 Freiburg, Germany

rapid device optimization, as deposition recipes must be tailored to each substrate. Consequently, direct comparisons across different hole transport layers (HTLs) are not possible using this deposition method.

Furthermore, we highlight the intrinsic challenges associated with controlling the deposition rates of inorganic precursors due to the crosstalk caused by the non-linear evaporation behaviour of organic precursors. This imbalance complicates the precise control of the targeted perovskite composition, ultimately leading to significant reproducibility challenges in the thermal co-evaporation process.

2 Influence of different hole transport layers (HTLs) on the co-evaporated perovskite properties

Here, we investigate the impact of different hole transport layers (HTLs) on the co-evaporation of organic–inorganic precursors from four distinct crucibles targeting a wide bandgap perovskite to be implemented as a top cell for tandem application. The four precursors used are cesium bromide (CsBr), lead bromide ($PbBr_2$), lead iodide (PbI_2) and formamidinium iodide (FAI). The recipe can be found in Fig. S1(a). The objective is to fabricate a double-cation, double-halide perovskite with the composition ($FA_xCs_{1-x}Pb(I_yBr_{1-y})_3$) targeting a bandgap of 1.68 eV.

The initial investigation aimed to compare the electrical properties of different HTLs and their suitability with the co-evaporated perovskite. However, to our surprise, we found that the co-evaporated perovskite exhibits a strong substrate dependence beyond electrical characteristics. Fig. 1 illustrates the influence of different underlying HTLs on perovskite formation. Perovskite films grown on different HTLs show different optical appearances (black color on TaTm/Spiro-TTB/bare glass, and yellow on all carbazole-based self-assembled molecules (SAMs)). This colour difference suggests the formation of different crystallographic phases depending on the underlying HTL. We confirmed this using X-ray diffraction (XRD) (Fig. S4 and S5).

Perovskite films grown on TaTm and Spiro-TTB formed a pure perovskite alpha phase (compare XRD findings in Fig. S5). Conversely, the layer grown on carbazole-based HTLs (*i.e.* 2PACz, MeO-2PACz and Me-4PACz) exhibited mixed phases. In addition to the alpha phase peak at $2\theta = 14°$, an additional peak at $2\theta = 10°$ was observed, corresponding to the orthorhombic delta phase (Fig. S4). Furthermore, diffraction peaks at $2\theta = 24.7°$ and $25.6°$ were identified on all carbazole-based HTLs, indicating the existence of a monoclinic FAI crystal structure (zoomed in XRD in Fig. S6).[14,15] This suggests that more FAI is incorporated into the films grown on carbazole-based HTLs. To further confirm the extra incorporation of FAI on SAMs, we performed energy dispersive X-ray (EDX) analysis (Fig. S7). The results are in agreement with XRD, showing that

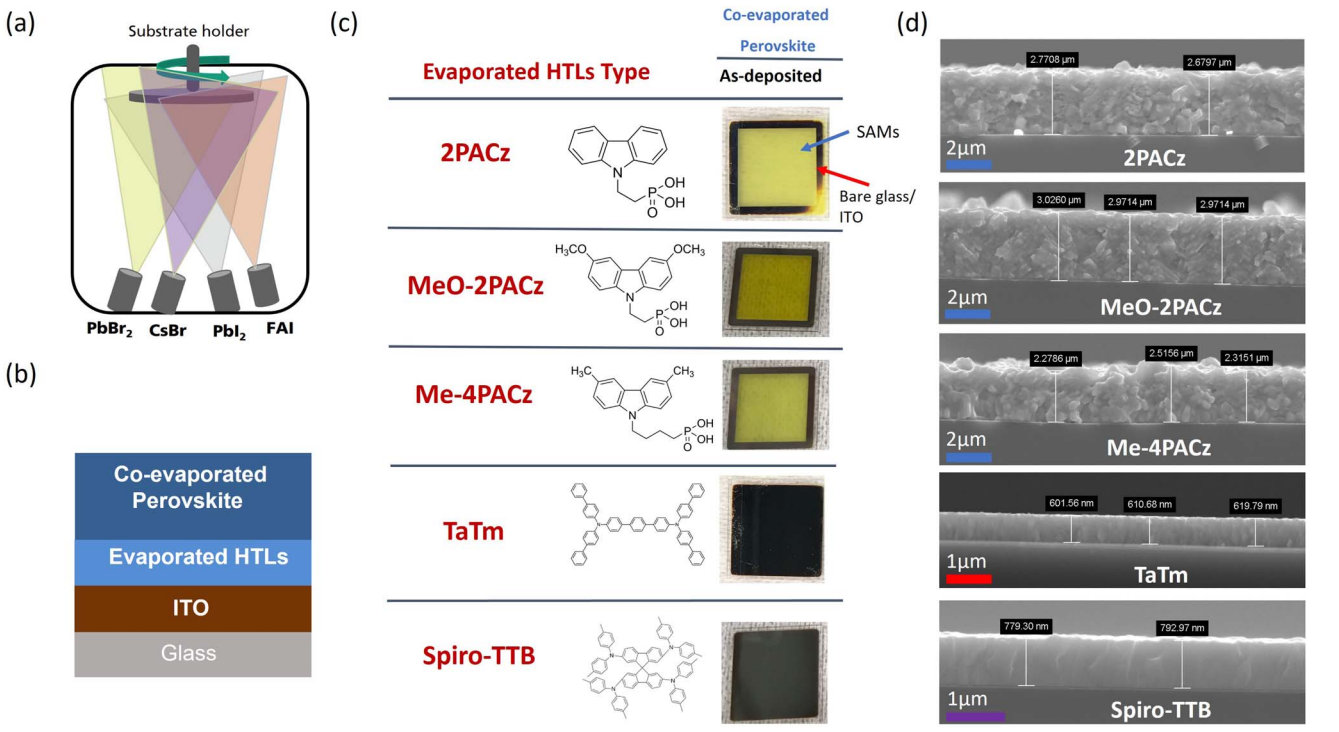

Fig. 1 (a) Schematic of the evaporation chamber used for co-evaporation of organic–inorganic precursors (recipe in Fig. S1(a)). (b) Schematic of the layer stack used to study the co-evaporation processes. (c) Overview of the used HTL materials and photographs of the resulting perovskite samples. During evaporation of the SAMs, a physical mask is required to hold the substrates, leading to partial coverage and leaving a rim on the sample without SAM deposition. (d) Cross-section SEM images of co-evaporated perovskite on different HTLs. The same recipe results in significant differences in morphology, phases and thickness.

more FAI is incorporated into the absorber film when carbazole based SAMs are used as HTLs.

FAI peaks (XRD) and high FAI signals (EDX) detected for all carbazole-based HTLs might also explain the difference in the overall co-evaporated perovskite thicknesses. In addition to optical and structural differences, the morphology and thickness of the co-evaporated perovskite exhibit significant variations depending on the underlying substrate (Fig. 1(d)). Notably, all carbazole-based HTLs resulted in perovskite films with poor morphology and unexpectedly large thicknesses of around 3 μm. In contrast, perovskite films deposited on TaTm and Spiro-TTB exhibited a more columnar growth pattern with substantially reduced thicknesses of less than 1 μm.

Furthermore, annealing the samples did not induce any visible changes in optical appearance (Fig. S8), suggesting that no phase transition occurred during thermal treatment. This observation is further supported by XRD analysis (Fig. S4 and S5). Thicknesses remained similar after annealing (Fig. S9).

3 Influence of different HTLs on the evaporated FAI

To investigate the excess FAI incorporation observed on carbazole-based HTLs, we deposited only FAI on different HTLs. Since previous studies showed no variation in inorganic precursor thickness across HTLs (Fig. S5 in ref. 16), only the organic precursor FAI was used (see recipes in Fig. S3). 2PACz was used as a representative example of a carbazole-based HTL. The HTL was evaporated and spin-coated to assess whether the deposition method had an influence. Additionally, a variation in the washing step was introduced to study the impact of the density of phosphonic acid groups on the formation of FAI. For all spin-coated 2PACz samples, the standard annealing treatment[17] was carried out: annealing at 100 °C for 10 minutes inside a nitrogen-filled glove box.

Despite depositing only FAI, sensors from other crucibles also detected some deposition rates as depicted in Fig. 2(d) and S3(a). This indicates that FAI does not evaporate in a directional cone from the crucible, as is often assumed (Fig. 2(a)). Instead it is able to also reach the quartz crystal microbalances (QCMs) of the other deposition sources causing unwanted cross-talk between the different QCMs (Fig. 2(b)). This makes it impossible to control and fine-tune the individual rates, a basic requirement for proper co-evaporation of perovskite (also see Fig. S10).

We investigated the thickness and morphology of FAI films on different HTLs using cross-sectional SEM (Fig. 3(c) and S11). A clear correlation was observed between FAI thickness and the surface density of phosphonic acid groups: non-washed 2PACz showed the thickest FAI layer, washed 2PACz a thinner one, and Spiro-TTB and TaTm the thinnest, consistent with their lack of phosphonic acid groups. Water contact angle measurements supported these findings, showing higher angles for washed 2PACz, Spiro-TTB, and TaTm, indicating reduced or absent phosphonic acid group density (Fig. 3(a) and S12).

The top-view SEM images of FAI deposited on different substrates reveal a higher density of grain boundaries on washed SAMs compared to their non-washed counterparts (Fig. 3(b) and S13). This observation correlates with the increased contact angle with lower density of phosphonic acid groups on the surface. Reaching an extreme case where phosphonic acid is entirely absent, such as in the case of Spiro-TTB and TaTm, the contact angle is substantially higher, leading to the formation of discrete FAI islands rather than a continuous film (Fig. 3(b)).

To further ensure that the contact angle with FAI mirrors that observed with water molecules and to prove the hypothesis that hydrogen bonding dictates the interaction between FAI and the different HTLs, we evaporated only a few nanometers of FAI on a substrate rich in phosphonic acid groups (2PACz). We then compared it with the island formation of FAI on a surface that contains none (Spiro-TTB) (recipe in Fig. S3(b)).

The aim of this simple experiment is to compare the contact angle of FAI with the different HTLs. The results, presented in Fig. 4, reveal a stronger interaction between FAI and phosphonic acid groups leading to a lower contact angle with 2PACz

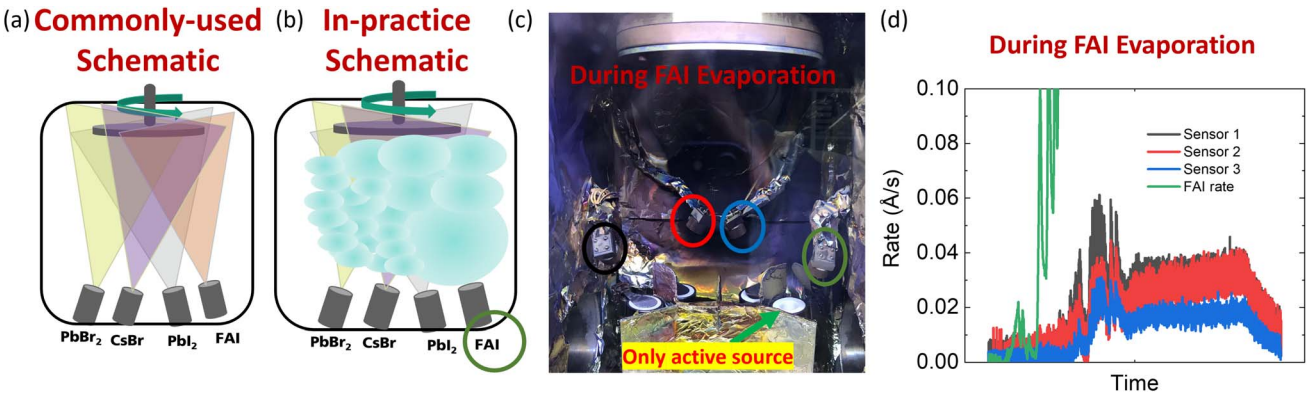

Fig. 2 (a) Commonly used schematic of evaporated FAI (false schematic). (b) In-practice schematic of evaporated FAI showing a more realistic scenario for how FAI deviates from this cone shape in (a) to form a cloud shape. (c) Inside the evaporation chamber showing the FAI cross-talk with the other crucible sensors in red arrows (quartz crystal microbalance (QCM) shown in circles; different colors correspond to the numbers of sensors in (d)). (d) Rates detected by other QCMs when only FAI is evaporated (more in Fig. S3(a)).

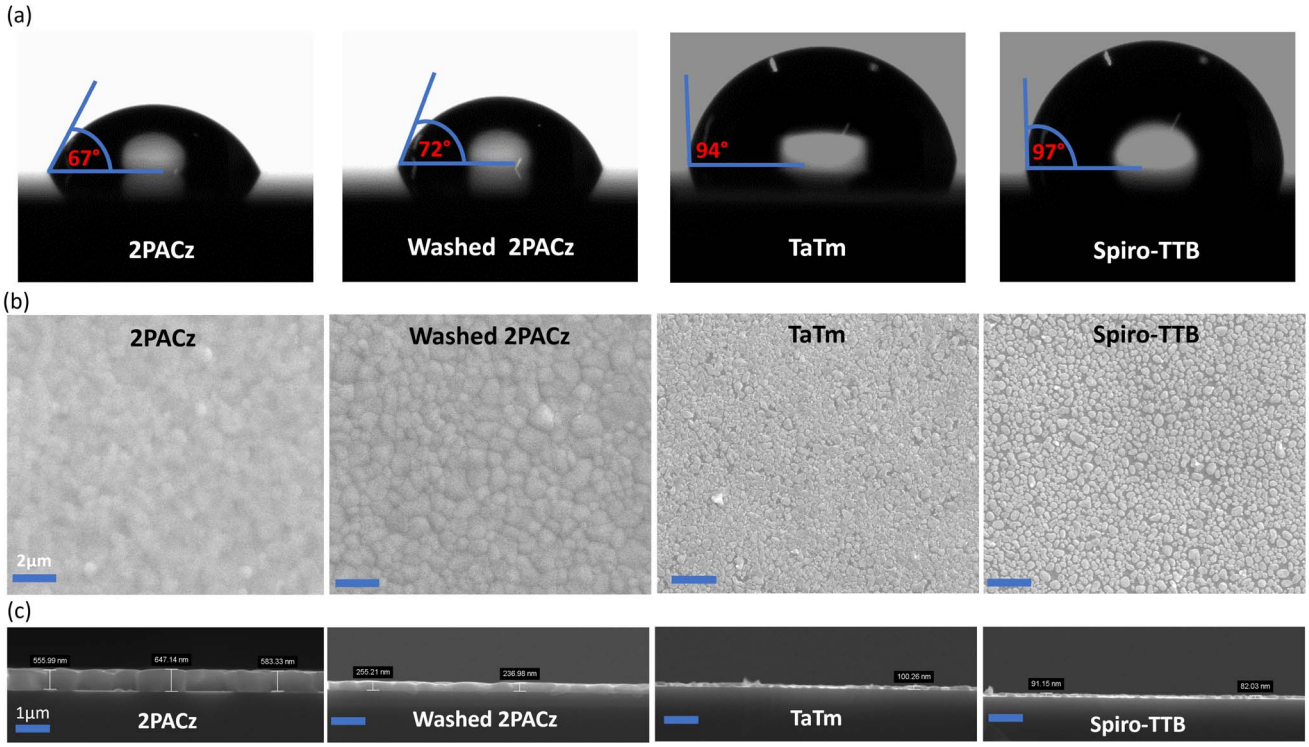

Fig. 3 (a) Contact angle measurement of deionized water on different HTLs. The angle formed between the water droplet and the surface indicates the strength of the hydrogen bond formed between the surface of the substrate and water. The higher contact angle suggests less wettability, and a more hydrophobic surface indicating less hydrogen bond formation. The average values of several droplets deposited on two samples are shown in the image. Additional data can be found in Fig. S10. (b) SEM top view images of FAI deposited on different HTLs. More grain boundaries for the deposited FAI films are observed on substrates that have a lower amount of phosphonic acid groups (surfaces with a high contact angle). (c) SEM cross-section images of FAI deposited on different HTLs revealing thinner FAI on low phosphonic acid density surfaces (surfaces with a high contact angle).

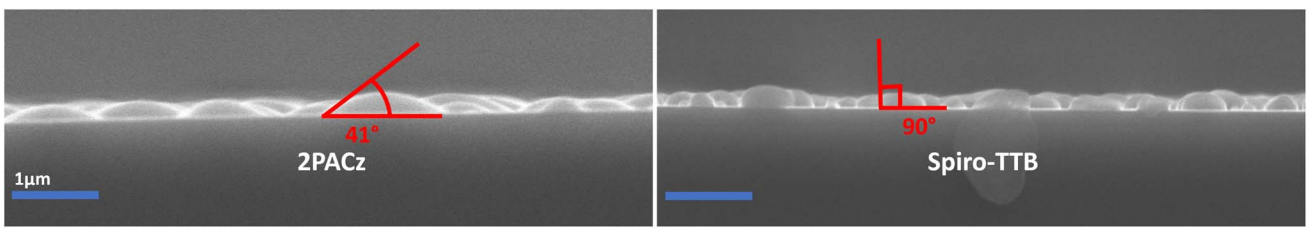

Fig. 4 Cross-section SEM images of evaporated FAI on two different HTLs. The contact angle formation of the first few nanometers of FAI on 2PACz is lower than that of Spiro-TTB just as seen with water in Fig. 3(a). The contact angle was measured using the software image J. The tilted scan is presented in Fig. S12.

than Spiro-TTB, exhibiting the same behaviour as water on the different HTLs. This reveals that the interaction inside the evaporation chamber imitates the same behaviour as dropping water molecules on these different surfaces.

In the literature possible hydrogen bonds between different constituents have been discussed. This included possible hydrogen bonding between the FA^+ cation and phosphonic acid groups.[12] Several publications mentioned the hydrogen bond between FAI and phosphonic acid groups.[6,12] However, recent literature[13] supports only the hydrogen bond of iodine with the phosphonic acid groups.

4 Influence of washed SAMs on the co-evaporated perovskite properties

To further confirm the correlation between different FAI incorporation amounts based on the density of phosphonic acid groups, we compared co-evaporated perovskite growth on washed and unwashed 2PACz layers. The as-deposited 2PACz was washed, and the co-evaporation time was reduced from 110 min to 60 min (recipe in Fig. S1(b)), as the longer time produced ~3 µm-thick films (Fig. 1). As shown in Fig. S14(c), films on washed 2PACz were thinner (~920 nm) than those on unwashed 2PACz (~1.5 µm), confirming that reduced

phosphonic acid group density significantly reduces perovskite thickness due to lower FAI incorporation as shown previously.

Besides the thickness differences, the co-evaporated films deposited on the washed 2PACz exhibited a darker film in comparison to the non-washed substrates (Fig. S14). This can indicate that the excess of FAI might be contributing to a non-pure alpha phase that was also found previously on the non-washed carbazole based HTLs. Later, we show that excess FAI is the main reason for the yellowish optical appearance of the films which were supported by the presence of mixed phases and FAI phases in XRD. In addition, we observe no difference in the formation of perovskite between evaporated and spin-coated 2PACz (Fig. S14(c)). This is in line with our earlier described observations of the FAI thickness on the different HTLs (Fig. S11).

We reduced the time of evaporation and the FAI rate further with the aim to obtain both reasonable thicknesses and a pure perovskite alpha phase on SAMs, respectively (recipe in Fig. S2(b)). Notably, for the first time, a pure alpha phase was observed on the washed SAM substrate (Fig. 5). This shows clearly the relation between the amount of FAI incorporated and the resulting pure alpha perovskite phase. Excess FAI is the reason for a non-pure alpha phase (resulting in a yellowish film due to non-photoactive phases and the FAI phase). The absorber films on non-washed SAM substrates had a high amount of incorporated FAI as confirmed by XRD (Fig. S16) and exhibited a higher thickness (determined from SEM measurements in Fig. S17).

This shows a lower amount of evaporated FAI is needed especially when substrates that are rich in phosphonic acid groups are used since FAI incorporation increases.

Within the same evaporation run, we added substrates with TaTm and Spiro-TTB (Fig. S18). We found that the bandgap is higher on the TaTm and Spiro-TTB samples (Fig. S19) compared to the washed SAMs, which was further supported by the Tauc plot in Fig. S20 and S21 extracted from the transmission-reflection measurements. This increase is likely due to the higher incorporation of FAI on the washed SAM substrate compared to Spiro-TTB and TaTm (as we proved earlier in Fig. 3(c)), which in turn increased the iodide to bromide ratio. This is also shown with the lower thicknesses of perovskite on Spiro-TTB and TaTm (SEM cross-section in Fig. S23) which was 210 nm, while 265 nm were deposited on washed 2PACz as shown previously (SEM coss-section in Fig. S17).

These findings reveal that perovskite formation strongly depends on the underlying HTL. Even with optimized recipes yielding the alpha phase on washed SAMs and non-carbazole-based HTLs (Spiro-TTB and TaTm), bandgap variations persist due to differing FAI incorporation levels.

Following the investigations outlined above, it is evident that variations in the HTLs—including treated substrates, such as washing or annealing as discussed later—result in different perovskite formations with completely different properties. This poses a challenge when conducting a systematic study or comparing the electrical behavior of different HTLs. Specifically, it is not possible to co-evaporate perovskite within a single run using the same recipe on different HTLs, as each substrate material/treatment requires the development of an optimized recipe. Besides, the same run results in different perovskite properties, *i.e.* irreproducible from one run to another as we see also later. This makes rapid device-level improvement difficult and limits the reliability of this deposition method.

5 Practical challenges in co-evaporating perovskite for perovskite-silicon tandem solar cells

Since Spiro-TTB and TaTm showed an alpha phase structure with 1.64 eV (Fig. S18 and S19), we chose to proceed with the same co-evaporation recipe run on both HTLs, as the bandgaps are within the optimal range for use as a top cell in a tandem solar cell with silicon as a bottom cell.

Perovskite solar cells were subsequently fabricated with the optimised recipe from Fig. S2(b). We increased the evaporation time from 40 min to 80 min to increase the perovskite thickness to reach current matching conditions for the 1.64 eV bandgap. More about relation of thickness and bandgap for current matching with the silicon sub cell can be found in ref. 18. The perovskite was tested in both as-deposited and annealed states to investigate the effect of annealing on the structural and optoelectronic properties of the co-evaporated perovskite.

The results reveal that annealing affects the structural and optoelectronic properties of the co-evaporated perovskite, irrespective of the type of HTL (Fig. S25). Specifically, a notable increase in the bandgap was observed upon annealing for both HTLs. This effect is evident in the XRD measurements by the shift of the main perovskite peak towards higher angles (Fig. S25(d)) and from the bandgap extracted from the peak position of spectrally resolved photoluminescence (PL) measurements (Fig. S25(a)).

Furthermore, a slight increase in the implied open circuit voltage (iV_{OC}) for the samples with TaTm as the HTL is observed compared to samples with Spiro-TTB as the HTL (Fig. S25(b)). This increase in iV_{OC}, particularly for the annealed samples, can be attributed to the enhanced perovskite crystallinity when

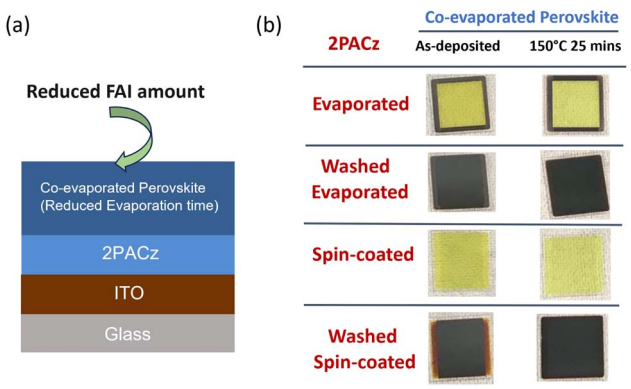

Fig. 5 (a) Schematic of the layer stack used to study co-evaporation of organic–inorganic precursors on 2PACz (evaporated and spin-coated) and washed 2PACz (co-evaporation recipe in Fig. S2(b)). (b) Darker films on washed substrates.

TaTm is used as one can see a stronger perovskite formation in the main perovskite peak in the XRD data (*i.e.* narrower FWHM). The improved crystallinity and the lower grain boundary density were demonstrated in previous work to suppress the non-radiative recombination, improving iV_{OC}.[19,20]

It is crucial to note that the evaporation process, which previously resulted in a bandgap of 1.64 eV (Fig. S19) has yielded a different bandgap in this instance, as shown in Fig. S25. This discrepancy highlights the irreproducibility, which is primarily attributed to the inability to control the evaporation rates from the other crucibles during the FAI deposition process. In other words, even if the measured rates are controlled, we do not know what portion of the measured rates from the inorganic crucibles corresponds to FAI (due to cross-talk from FAI). This further impedes device development and reduces reliability.

To assess the device performance of the tandem solar cells we measured their current-voltage *jV* characteristics (Fig S26). For the samples with as-deposited perovskite, Spiro-TTB shows a better performance on average than TaTm. The samples from both groups with different HTLs show a slight decrease in the open circuit voltage V_{OC} upon annealing. The difference in performance between the two HTLs can be attributed to the different perovskite crystallization especially upon annealing (Fig. S25(c) and (d)) as well as to the different energy alignment between the valence band and the HOMO level of the HTLs as revealed by cyclic voltammetry (CV) (Fig. S27). More about the CV characterization can be found in the SI and ref. 21.

In general, the current remained relatively low across all samples, which can be explained by a significant imbalance in the generated current between the two subcells of the tandem device. To investigate this imbalance, quick spectrometric measurements were conducted, as described in ref. 22. The measurements were done on the tandem cell with TaTm as a HTL and annealed perovskite. The top cell is strongly current limiting, as depicted in Fig. S28 (sample with a green inverted triangle label). This limitation is primarily due to the high bandgap of the top cell (unplanned due to irreproducibility as discussed before) and its relatively low thickness, which is approximately 450 nm, as confirmed by the SEM images in Fig. S24.

From *jV* curves, we observed low breakdown voltage in the cells. The rise in the current at $V = 0$ could be due to the breakdown of the perovskite subcell. The tandem solar cell is limited by the current of the perovskite as revealed by metric measurements (Fig. S28). Therefore, under j_{SC} condition of the tandem the perovskite is operating at a negative voltage, and if this negative voltage is higher than the breakdown voltage of the perovskite, it breaks down. For more elaboration on that, we refer to this article.[23]

Following the previous results and in an attempt to improve the conductivity of the HTLs, both HTLs were annealed prior to the perovskite deposition. The motivation to anneal the HTLs for enhanced conductivity is derived from the findings of the study by Babaei *et al.*[24] However, in their work, the authors employed a bilayer structure as the HTL.

The HTLs (prior the co-evaporation) were annealed inside a glovebox (N_2 environment) for 10 mins at 140 °C. The co-evaporated perovskite remained as-deposited for both groups.

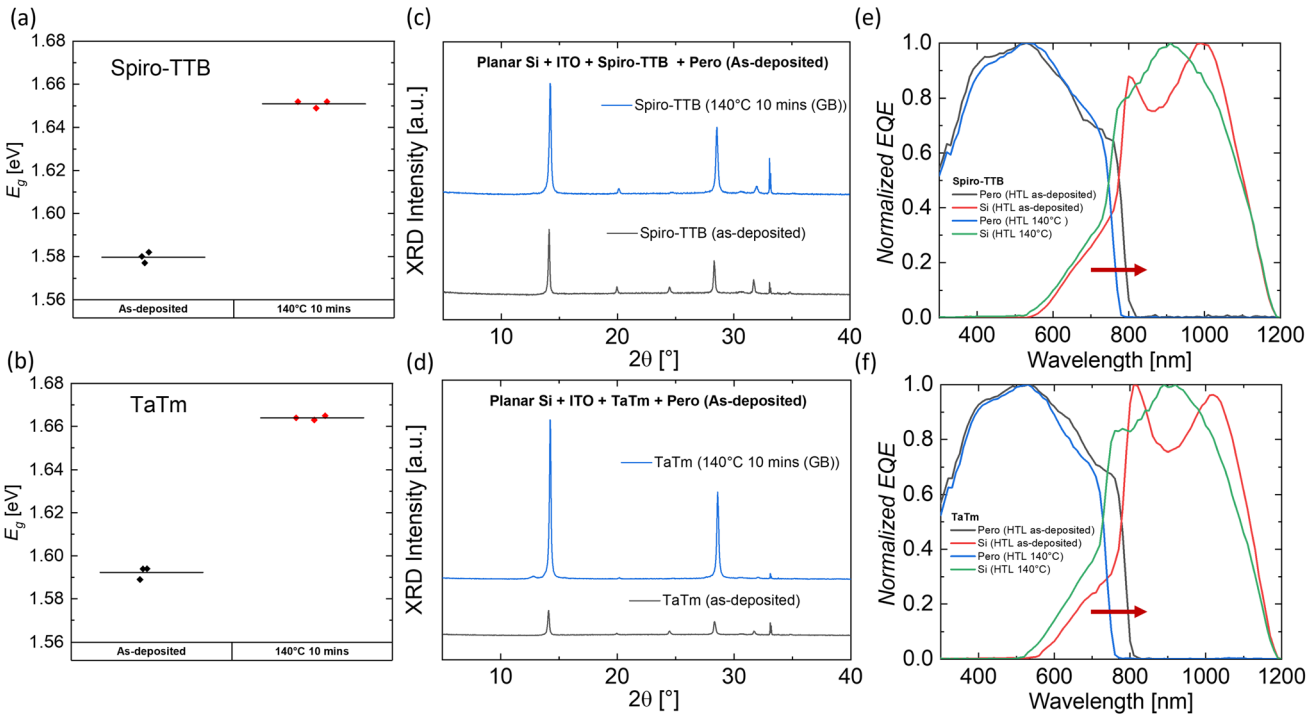

Fig. 6 (a and b) Bandgap of co-evaporated perovskite extracted from the peak position of spectrally resolved PL measurements on the different treated HTLs (annealed at 140 °C for 10 min in a nitrogen-filled glovebox) and as-deposited HTLs. (c and d) XRD of co-evaporated perovskite on the different HTLs. (e and f) Normalized EQE of the tandem solar cell using the different HTLs showing the different bandgaps of the perovskite with a red arrow.

Perovskite films evaporated onto the annealed HTLs showed similar thicknesses to the as-deposited HTLs (Fig. S29).

However, the electrical and structural characterization studies of the perovskite showed a substantial difference between the substrates that are annealed and the ones that are not prior to the co-evaporation process (Fig. 6). We extracted the bandgap from the peak position of spectrally resolved PL measurements in Fig. 6 which supports a bandgap shift of the perovskite grown on the different treated HTLs. The perovskite films on both as-deposited HTLs exhibit a significantly low bandgap, which is too low to be suitable for use as a top cell in tandem with silicon. We confirmed the bandgap shift also in the EQE as shown by the red arrows in Fig. 6(e) and (f).

Additionally, the influence of the altered bandgap and the improved perovskite crystallinity on the treated HTLs on the device performance was evident in the overall performance of the tandem devices, as depicted in Fig. S30. Furthermore, we tracked the efficiency of the champion device (from Fig. S30(a)). After storage in a nitrogen-filled glovebox the power conversion efficiency had increased from initially 21.5% to 22% (Fig. S31). This might show the potential stability of perovskite films fabricated *via* the co-evaporation route, with no use of solvents in the entire top cell stack.

Additionally, the cell is slightly silicon limited as shown in Fig. S28 (orange squares) meaning that we can also still gain current and voltage by slightly increasing the bandgap of the perovskite. However, to establish co-evaporation as a reliable deposition method for perovskite films, it is crucial to address the challenges discussed in this study, particularly the need for a more consistent and controllable deposition process for FAI. However, even with an ideal, controllable FAI deposition technique, recipes would still need to be adjusted for each HTL making it an inherent limitation for this deposition method.

6 Conclusions

In this study, we demonstrated that the substrate material critically influences the properties of co-evaporated hybrid organic–inorganic perovskite films. The interaction between phosphonic acid groups and evaporated formamidinium iodide (FAI) was found to resemble that with water. We further showed that post-treatments of the HTL such as annealing and washing, even on identical substrates, significantly affect key perovskite features, including the bandgap, thickness, and crystallinity. Moreover, we established a clear correlation between FAI content and perovskite phase formation, with excess FAI suppressing the pure alpha phase. Challenges arising from the non-directional evaporation of FAI were also identified, limiting reproducibility. These insights are particularly relevant for the co-evaporation method, which offers advantages such as solvent-free processing, improved film uniformity, and compatibility with various substrates. To advance co-evaporation as a reliable fabrication route, future work should focus on precise FAI deposition control—best addressed through improved evaporation chamber design rather than solely material optimization. Nevertheless, even with enhanced chamber designs, our results emphasize that co-evaporation recipes must be specifically tailored to each substrate material. This is an inherent limitation for this deposition method.

Author contributions

Mohamed A. A. Mahmoud (conceptualization: lead; data curation: lead; formal analysis: lead; investigation: lead; methodology: lead; visualization: lead; writing – original draft: lead; writing – review & editing: lead). Yashika Gupta (supervision: supporting; writing – review & editing: supporting). Oliver Fischer (investigation: supporting; writing – review & editing: supporting). Jann B. Landgraf (investigation: supporting; writing – review & editing: supporting). Martin Bivour (resources: supporting; writing – review & editing: supporting). Juliane Borchert (resources: lead; supervision: lead; writing – review & editing: supporting).

Conflicts of interest

There are no conflicts to declare.

Data availability

The data supporting this article have been included as part of the supplementary information (SI). Supplementary information is available. See DOI: https://doi.org/10.1039/d5ta08316h.

Acknowledgements

The authors would like to thank Karin Zimmermann and Henning Nagel for silicon bottom solar cell processing, Almudena Gonzalez and Yannik Schmidt for EQE measurements, and Jithin Shaji for RTA and JV measurements. The authors would like to thank Alexander J. Bett for fruitful discussion regarding the EQE interpretation. Futhermore, the authors would like to thank Konrad Fischer and Jacob Myers for technical support. We would also like to thank the Vector Stiftung and Deutsche Forschungsgemeinschaft (DFG, German Research Foundation) under Germany's Excellence Strategy – EXC-2193/1 – 390951807 for funding this work.

Notes and references

1 F. U. Kosasih, E. Erdenebileg, N. Mathews, S. G. Mhaisalkar and A. Bruno, *Joule*, 2022, **6**, 2692–2734.
2 M. Piot, J. E. S. Alonso, K. P. S. Zanoni, N. Rodkey, F. Ventosinos, C. Roldán-Carmona, M. Sessolo and H. Bolink, *ACS Energy Lett.*, 2023, **8**, 4711–4713.
3 T. C.-J. Yang, T. Kang, M. Fitzsimmons, G. Vega, Y. Lu, L. Rosado, A. Jiménez-Solano, L. Pan, S. J. Zelewski, J. Ferrer Orri, Y.-H. Chiang, D. Guo, Z. Y. Ooi, Y. Han, W. Xu, B. Roose, C. Ducati, S. Carretero Palacios, M. Anaya and S. D. Stranks, *EES Sol.*, 2025, **1**, 41–55.
4 S. Yan, J. B. Patel, J. E. Lee, K. A. Elmestekawy, S. R. Ratnasingham, Q. Yuan, L. M. Herz, N. K. Noel and M. B. Johnston, *ACS Energy Lett.*, 2023, **8**, 4008–4015.

5 J. Feng, Y. Jiao, H. Wang, X. Zhu, Y. Sun, M. Du, Y. Cao, D. Yang and S. F. Liu, *Energy Environ. Sci.*, 2021, **14**, 3035–3043.
6 M. Roß, S. Severin, M. B. Stutz, P. Wagner, H. Köbler, M. Favin-Lêque, A. Al-Ashouri, P. Korb, P. Tockhorn, A. Abate, B. Stannowski, B. Rech and S. Albrecht, *Adv. Energy Mater.*, 2021, **11**, 2101460.
7 Y.-Y. Xu, Y. Jiang, H.-Q. Du, X. Gao, Z.-Y. Qiang, C.-X. Wang, Z.-W. Tao, L.-H. Yang, R. Zhi, G.-J. Liang, H.-Y. Cai, M. U. Rothmann, Y.-B. Cheng and W. Li, *Adv. Funct. Mater.*, 2024, **34**, 2312037.
8 T. Abzieher, T. Feeney, F. Schackmar, Y. J. Donie, I. M. Hossain, J. A. Schwenzer, T. Hellmann, T. Mayer, M. Powalla and U. W. Paetzold, *Adv. Funct. Mater.*, 2021, **31**, 2104482.
9 S. Chozas-Barrientos, A. Paliwal, F. Ventosinos, C. Roldán-Carmona, L. Gil-Escrig, V. Held, P. Carroy, D. Muñoz and H. J. Bolink, *ACS Energy Lett.*, 2025, 1733–1740.
10 V. Škorjanc, A. Miaskiewicz, M. Roß, S. Maniyarasu, S. Severin, M. R. Leyden, P. Holzhey, F. Ruske, L. Korte and S. Albrecht, *ACS Energy Lett.*, 2024, **9**, 5639–5646.
11 M. Roß, L. Gil-Escrig, A. Al-Ashouri, P. Tockhorn, M. Jošt, B. Rech and S. Albrecht, *ACS Appl. Mater. Interfaces*, 2020, **12**, 39261–39272.
12 H. Xie, Z. Wang, Z. Chen, C. Pereyra, M. Pols, K. Gałkowski, M. Anaya, S. Fu, X. Jia, P. Tang, D. J. Kubicki, A. Agarwalla, H.-S. Kim, D. Prochowicz, X. Borrisé, M. Bonn, C. Bao, X. Sun, S. M. Zakeeruddin, L. Emsley, J. Arbiol, F. Gao, F. Fu, H. I. Wang, K.-J. Tielrooij, S. D. Stranks, S. Tao, M. Grätzel, A. Hagfeldt and M. Lira-Cantu, *Joule*, 2021, **5**, 1246–1266.
13 T. Feeney, J. Petry, A. Torche, D. Hauschild, B. Hacene, C. Wansorra, A. Diercks, M. Ernst, L. Weinhardt, C. Heske, G. Gryn'ova, U. W. Paetzold and P. Fassl, *Matter*, 2024, **7**, 2066–2090.
14 A. A. Petrov, E. A. Goodilin, A. B. Tarasov, V. A. Lazarenko, P. V. Dorovatovskii and V. N. Khrustalev, *Acta Crystallogr., Sect. E*, 2017, **73**, 569–572.
15 K. L. Heinze, T. Schulz, R. Scheer and P. Pistor, *Phys. Status Solidi A*, 2024, **221**, 2300690.
16 B. P. Kore, O. Er-raji, O. Fischer, A. Callies, O. Schultz-Wittmann, P. S. C. Schulze, M. Bivour, S. De Wolf, S. W. Glunz and J. Borchert, *Energy Environ. Sci.*, 2025, **18**, 354–366.
17 A. Al-Ashouri, A. Magomedov, M. Roß, M. Jošt, M. Talaikis, G. Chistiakova, T. Bertram, J. Marquez-Prieto, E. Köhnen, E. Kasparavičius, S. Levcenco, L. Gil-Escrig, C. Hages, R. Schlatmann, B. Rech, T. Malinauskas, T. Unold, C. A. Kaufmann, L. Korte and S. Albrecht, *Energy Environ. Sci.*, 2019, **12**(11), 3356–3369.
18 M. Heydarian, C. Messmer, A. J. Bett, M. Heydarian, D. Chojniak, Ö. Ş. Kabaklı, L. Tutsch, M. Bivour, G. Siefer, M. C. Schubert, J. C. Goldschmidt, M. Hermle, S. W. Glunz and P. S. C. Schulze, *Sol. RRL*, 2023, **7**, 2200930.
19 M. A. A. Mahmoud, O. Er-Raji, B. P. Kore, M. Bivour, P. S. C. Schulze, S. W. Glunz, A. W. Bett and J. Borchert, *Sol. RRL*, 2024, **8**, 2400471.
20 O. Er-raji, M. A. Mahmoud, O. Fischer, A. J. Ramadan, D. Bogachuk, A. Reinholdt, A. Schmitt, B. P. Kore, T. W. Gries, A. Musiienko, O. Schultz-Wittmann, M. Bivour, M. Hermle, M. C. Schubert, J. Borchert, S. W. Glunz and P. S. Schulze, *Joule*, 2024, **8**, 2811–2833.
21 J. B. Landgraf, Y. Gupta, A. Prasetio, S. Lange, C. Messmer, C. Schwarz, O. Fischer, S. Chanthalavong, O. Er-raji, M. B. Camarada, S. De Wolf, P. S. C. Schulze, A. Fischer, S. W. Glunz and J. Borchert, *Adv. Funct. Mater.*, 2025, e08186.
22 O. Fischer, A. J. Bett, K. Abrorov, M. A. A. Mahmoud, F. Schindler, S. W. Glunz and M. C. Schubert, *Sol. RRL*, 2008, **8**, 2400686.
23 M. Heydarian, A. J. Bett, C. Messmer, J. Aulich, O. Fischer, M. Heydarian, Y. Gupta, P. S. C. Schulze, J. Borchert, F. Schindler, M. C. Schubert and S. W. Glunz, *Sol. RRL*, 2024, **8**, 2400376.
24 A. Babaei, K. P. S. Zanoni, L. Gil-Escrig, D. Pérez-del Rey, P. P. Boix, M. Sessolo and H. J. Bolink, *Front. Chem.*, 2020, **7**, 936.

